



Universal material trends in extraordinary magnetoresistive devices

Erlandsen, Ricci; Pomar, Thierry Désiré; Kornblum, Lior; Pryds, Nini; Bjørk, Rasmus; Christensen, Dennis Valbjørn

Published in:
Journal of Physics: Materials

Link to article, DOI:
[10.1088/2515-7639/acfac0](https://doi.org/10.1088/2515-7639/acfac0)

Publication date:
2023

Document Version
Publisher's PDF, also known as Version of record

[Link back to DTU Orbit](#)

Citation (APA):
Erlandsen, R., Pomar, T. D., Kornblum, L., Pryds, N., Bjørk, R., & Christensen, D. V. (2023). Universal material trends in extraordinary magnetoresistive devices. *Journal of Physics: Materials*, 6(4), Article 045010. <https://doi.org/10.1088/2515-7639/acfac0>

General rights

Copyright and moral rights for the publications made accessible in the public portal are retained by the authors and/or other copyright owners and it is a condition of accessing publications that users recognise and abide by the legal requirements associated with these rights.

- Users may download and print one copy of any publication from the public portal for the purpose of private study or research.
- You may not further distribute the material or use it for any profit-making activity or commercial gain
- You may freely distribute the URL identifying the publication in the public portal

If you believe that this document breaches copyright please contact us providing details, and we will remove access to the work immediately and investigate your claim.



PAPER

OPEN ACCESS

RECEIVED

12 April 2023

REVISED

14 August 2023

ACCEPTED FOR PUBLICATION

18 September 2023

PUBLISHED

29 September 2023

Original Content from this work may be used under the terms of the [Creative Commons Attribution 4.0 licence](#).

Any further distribution of this work must maintain attribution to the author(s) and the title of the work, journal citation and DOI.



Universal material trends in extraordinary magnetoresistive devices

Ricci Erlandsen¹ , Thierry Désiré Pomar¹, Lior Kornblum² , Nini Pryds¹ , Rasmus Bjørk¹ and Dennis V Christensen^{1,*} ¹ Department of Energy Conversion and Storage, Technical University of Denmark, DK-2800 Kgs. Lyngby, Denmark² Andrew and Erna Viterbi Department of Electrical & Computer Engineering, Technion—Israel Institute of Technology, Haifa 32000-03, Israel

* Author to whom any correspondence should be addressed.

E-mail: dechr@dtu.dk**Keywords:** extraordinary magnetoresistance, magnetoresistance, magnetometers, graphene, semiconductor, oxides, electron mobilitySupplementary material for this article is available [online](#)

Abstract

Extraordinary magnetoresistance (EMR) is a geometric magnetoresistance emerging in hybrid systems typically comprising a high-mobility material and a metal. Due to a field-dependent redistribution of electrical currents in these devices, the electrical resistance at room temperature can increase by $10^7\%$ when applying a magnetic field of 5 T. Although EMR holds considerable potential for realizing sensitive, all-electronic magnetometers, this potential is largely unmet. A key challenge is that the performance of EMR devices depends very sensitively on variations in a vast parameter space where changes in the device geometry and material properties produce widely different EMR performances. The challenge of navigating in the large parameter space is further amplified by the poor understanding of the interplay between the device geometry and material properties. By systematically varying the material parameters in four key EMR geometries using diffusive transport simulations, we here elucidate this interplay with the aim of finding universal guidelines for designing EMR devices. Common to all geometries, we find that the sensitivity scales inversely with the carrier density, while the MR reaches saturation at low carrier densities. Increasing the mobility beyond $20\,000\text{ cm}^2\text{ Vs}^{-1}$ is required to observe strong EMR effects at 1 T with the optimal magnetoresistance observed for mobilities between $100\,000\text{--}500\,000\text{ cm}^2\text{ Vs}^{-1}$. An interface resistance below $\rho_c = 10^{-4}\text{ }\Omega\text{cm}^2$ between the constituent materials in the hybrid devices was also found to be a prerequisite for very high magnetoresistances in all geometries. By further simulating several high-mobility materials at room and cryogenic temperatures, we conclude that encapsulated graphene and InSb are amongst the most promising candidates for EMR devices showing high magnetoresistance exceeding $10^7\%$ below 1 T at room temperature. This study paves the way for understanding how to realize EMR devices with record-high magnetoresistance and high sensitivity for detecting magnetic fields.

1. Introduction

The discovery of extraordinary magnetoresistance (EMR) in 2000 showed great promise for applications requiring sensitive magnetometry, including read-heads for magnetic hard disks [1, 2], scanning magnetometry [3] and detection of biomagnetic fields [4–7]. The concept of EMR was pioneered by Solin *et al* who discovered extremely large magnetoresistances exceeding $10^6\%$ at room temperature in an applied magnetic field of 5 T [8]. The EMR effect is driven by the Lorentz force, which causes a field-induced current deflection in a hybrid device typically comprised of a high-mobility semiconductor joined with a highly conducting metal [8–10]. At zero magnetic field, the semiconductor-metal hybrid device resembles a short circuit where the majority of the current flows through the metallic region (see figure 1). When a magnetic field is present, the device assumes a state of high resistance as the current is deflected around the metallic

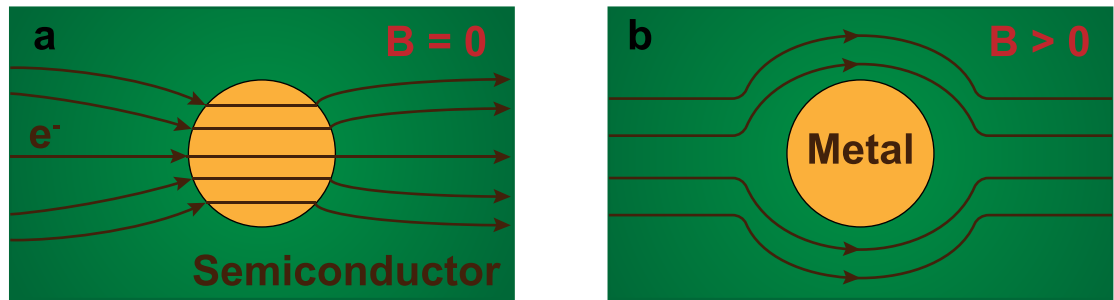


Figure 1. Schematic illustrations of the current flow in absence and presence of a magnetic field in a hybrid device comprising a highly conducting metal and a high-mobility semiconductor.

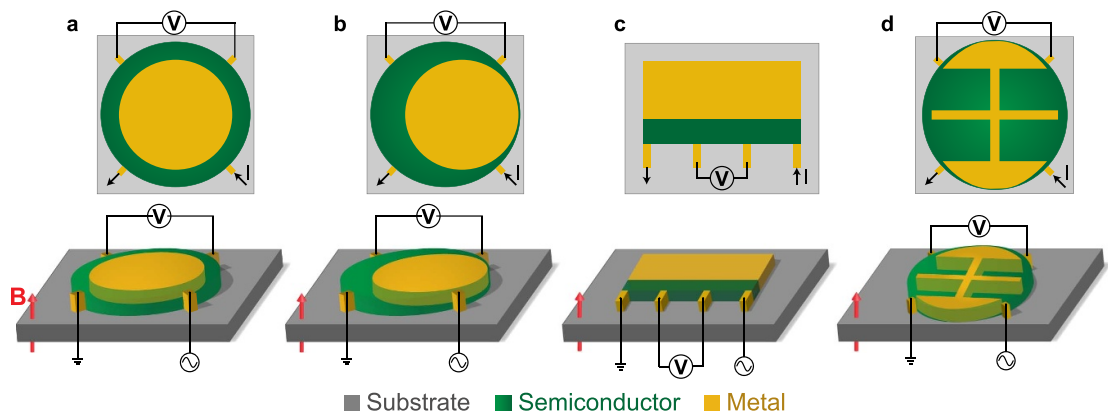


Figure 2. Schematic illustrations of four key extraordinary magnetoresistive device geometries: (a) Concentric circular device. (b) Asymmetric circular device. (c) Bar-shape device. (d) Multi-branched structure combined with ellipsoid edges.

region [11]. The deflection of the current is due to the distinct material properties in the individual regions of the hybrid device. In the metallic portion, a high electrical conductivity causes the entire volume to have a near-uniform electrical potential. As a result, the local electric field inside the device is always oriented perpendicular to the semiconductor/metal interface. In the absence of a magnetic field, the current follows the electric field lines and primarily travels through the metal region. However, when a magnetic field is applied, the resulting Lorentz force is tangential to this interface and deflects the current away from the metal, with the strength of this deflection increasing as a function of the applied magnetic field and mobility of the semiconductor. The EMR effect is pronounced both at room and low temperatures with the large magnetoresistance occurring in devices free of magnetic components and the associated magnetic noise and stray fields [11].

The EMR is a purely geometrical effect, however, it has been shown that some material parameters are important for determining the performance of EMR devices. Previous studies have explored the role of material properties by varying them with the use of finite element simulations and have found that achieving a high magnetoresistance generally requires a high electron mobility in the semiconductor, high electrical conductivity of the metal, as well as a low contact resistance between the two material regions [10, 12, 13]. In particular, for the benchmark concentric circular geometry, it was found that increasing the mobility from 500 to 200 000 $\text{cm}^2 \text{Vs}^{-1}$ increased the magnetoresistance at 1 T by three orders of magnitude, whereas the magnetoresistance completely vanished for high semiconductor/metal contact resistances [13]. The material requirements sparked an interest in studying the behavior of EMR in various high-mobility materials, including InSb [8, 12–17], InAs [18–20], GaAs [21–24] and graphene [25–30]. Beyond investigating different material platforms and material parameters, there has also been a strong interest in exploring various EMR geometries [2, 31–41]. Four of the key geometries explored for EMR are displayed in figure 2, which include the concentric circular devices, bar-shaped devices, the asymmetric off-center circular devices and more exotic multi-branched devices. As the EMR is a geometrical effect, reshaping the device geometry influences the magnetoresistive response dramatically [38–40]. The concentric circular and bar-shaped devices are the most commonly studied geometries and here a magnetoresistance up to $1.5 \cdot 10^6\%$ for InSb and $1 \cdot 10^7\%$ for

encapsulated graphene have been shown experimentally at $B = 5$ T [8, 30]. The devices are generally symmetric, leading to an overall symmetric magnetoresistance where $R(B) \approx R(-B)$, yielding a sensitivity of $dR/dB \rightarrow 0$ for $B \rightarrow 0$ T. In these devices, several studies report the effect of changing geometric parameters such as the semiconductor width and the area of the metal region [8, 18, 33, 35, 38, 42, 43]. The device symmetry is broken in the off-centered geometry, where simulations predict highly asymmetric magnetoresistance curves and a non-zero sensitivity ($dR/dB > 0$) towards weak magnetic fields [41]. Lastly, a few variants of branched structures, such as the one shown in figure 2(d), have also been investigated computationally, yielding a magnetoresistance of up to $10^{10}\%$ at 5 T [29, 38].

Both material parameters and device geometry thus play a crucial role in the performance of EMR. However, a universal understanding of the influence of material properties across various device geometries does not exist, and as a result a general set of guidelines for designing high-performing EMR devices is missing. For instance, whereas previous publications have reported both numerical [10, 33] and experimental [36] studies of the effects of material parameters, a universal approach that linked the geometric and material parameters was lacking. Here, we systematically vary the material parameters across the four key EMR geometries with the aim of identifying universal trends. From this, we gain a deeper understanding of the interplay between material and geometric parameters and propose a set of design guidelines applicable to realizing EMR devices with high magnetoresistance and sensitivity.

2. Methods

The use of a finite element model to describe diffusive transport in EMR devices was first reported by Moussa *et al* [9]. Their model was found to be in good agreement with both experimental data and an analytical solution that exists for the concentric circular device [44]. The method is discussed in detail elsewhere [2, 9, 10]. In our work, we reimplement the approach with the use of Comsol Multiphysics (v. 5.6) as described in a previous publication [41] and apply it to the four key EMR geometries illustrated in figure 2. The concentric circular device (figure 2(a)) was based on the work by Solin *et al* [8] with a filling factor $\alpha = r_i/r_o = 12/16$ where r_i and $r_o = 1$ mm are the radii of the inner metal and outer semiconductor circles, respectively. The filling factor was fixed to 12/16 as this gives a large magnetoresistance of $\sim 2 \cdot 10^5\%$ at 1 T and $\sim 450\%$ at 0.1 T [8, 39].

The asymmetric circular geometry (figure 2(b)) was based on our previous work [41] using $\alpha = 12/16$ with a 90% offset in the metallic inclusion. The dimensions used in the bar-shape device (figure 2(c)) were also based on previous work [35, 38] where it was shown that a length of $45 \mu\text{m}$, a semiconductor width of $3 \mu\text{m}$, a metal width of $15 \mu\text{m}$ and a voltage probe distance of $8 \mu\text{m}$ results in a maximal magnetoresistance at all magnetic fields. The multi-branched structure (figure 2(d)) was adapted from the work by Huang *et al* describing a Hall bar-like metal inclusion combined with ellipsoidal edges [38]. The edges drastically reduce the zero-field resistance as the current trajectory is primarily going through the highly conducting metallic inclusion, yielding the highest simulated magnetoresistance of $10^{10}\%$ at 5 T reported to date. The direction of the injected current (I) is depicted by the arrows for each device in figure 2. The model does not account for Joule heating or non-linear I/V curves, and the results shown are therefore invariant to the current magnitude. The voltage drop (ΔV) is probed between the voltage probes and is used to calculate the four-terminal resistance, $R = \Delta V/I$. The magnetic field dependence of the resistance is used to calculate the magnetoresistance (MR) as a function of the magnetic field, B , applied perpendicular to the device:

$$\text{MR} = \frac{R(B) - R(B=0)}{R(B=0)}. \quad (1)$$

The current flow is governed by Ohm's law, $\mathbf{j} = \boldsymbol{\sigma}\mathbf{E}$, where \mathbf{j} is the current density vector, $\boldsymbol{\sigma}$ is the conductivity tensor and \mathbf{E} is the electric field. The 3D conductivity tensor in the Cartesian coordinate system with i denoting the x , y or z direction is defined as:

$$\boldsymbol{\sigma}(B) = \frac{\sigma_0}{1 + (\mu B)^2} \begin{bmatrix} (1 + \beta_x^2) & (-\beta_z + \beta_y\beta_x) & (\beta_y + \beta_z\beta_x) \\ (\beta_z + \beta_y\beta_x) & (1 + \beta_y^2) & (-\beta_x + \beta_y\beta_z) \\ (-\beta_y + \beta_z\beta_x) & (\beta_x + \beta_y\beta_z) & (1 + \beta_z^2) \end{bmatrix}, \quad (2)$$

where β is the unitless magnetic field:

$$\beta = \mu B.$$

Here, μ is the electron mobility of the semiconductor, σ_0 is the Drude conductivity at $B = 0$ T given by:

$$\sigma_0 = ne\mu$$

where n is the carrier density and e is the fundamental charge. If transport in the z -direction can be neglected, the tensor can be reduced to two dimensions with the simpler form of:

$$\sigma(B) = \frac{\sigma_0}{1 + (\mu B)^2} \begin{bmatrix} 1 & -\mu B \\ \mu B & 1 \end{bmatrix}. \quad (3)$$

The numerical model solves the continuity equation of the electrostatic potential $\phi(x, y)$ under steady-state conditions:

$$\nabla \cdot [\sigma \nabla \phi(x, y)] = 0. \quad (4)$$

The default material parameters are based on the work by Solin *et al* [8], corresponding to a high-mobility InSb ($\sigma_s = 1.86 \cdot 10^4 \text{ S m}^{-1}$, $\mu = 45500 \text{ cm}^2 \text{ Vs}^{-1}$ and $n = 2.5 \cdot 10^{16} \text{ cm}^{-3}$ at room temperature) as the semiconducting material and gold ($\sigma_m = 4.52 \cdot 10^7 \text{ S m}^{-1}$, $\mu = 50 \text{ cm}^2 \text{ Vs}^{-1}$ and $n = 5.6 \cdot 10^{22} \text{ cm}^{-3}$ at room temperature) as the metal. The metal and the semiconductor are non-magnetic materials, which eliminates the noise and magnetic stray field associated with magnetic components when using EMR for magnetometry applications. Unless otherwise stated, the thickness of InSb and gold is set to $t = 1.3 \text{ }\mu\text{m}$ in the 2D model with $R \propto 1/t$. The metal contacts to the semiconductor are modeled as boundaries on the perimeter of the semiconducting disc with angular widths of 9° . As the devices are probed in four-terminal mode, contact resistances to the metal contacts were omitted. The Laplace equation (equation (4)) is then solved under the boundary condition that no current flows at the perimeter of the semiconductor disc, except for where the source and drain contacts are placed. The contact resistance was modeled as an Ohmic interface resistance between the metallic inclusion and the semiconductor, which neglects Schottky barriers or other sources of non-linearities. The contact resistance only takes nonzero values when explicitly stated. This is justified by the low contact resistance obtained experimentally as discussed later as well as the good match between the present model and the experimental data of InSb-based EMR devices in the absence of contact resistance and non-linear I/V characteristics. The sensitivity, dR/dB , was calculated by numerical differentiation using the central difference principle and a magnetic field resolution of 10 mT.

3. Variations in material parameters

For all of the modeled geometries (figure 2), we systematically vary a single parameter at a time while fixing the remaining parameters to the default values stated in the method section. The default values correspond to high-mobility InSb as the semiconductor, gold as the metal and no contact resistance between metal and semiconductor. First, we address universal trends across the four key EMR geometries by varying the semiconductor carrier density, carrier mobility and contact resistance independently. The material parameters are highly interdependent in real materials where, e.g. changing the carrier density generally greatly affects both the carrier mobility and contact resistance. This interdependence is intentionally omitted here to provide a clear picture of how the individual material parameters affect the EMR devices. Second, we simulate the expected performance using a variety of state-of-the-art high-mobility materials.

3.1. Carrier density

Figures 3(a)–(d) show the resistance as a function of magnetic field for the four different EMR geometries with the carrier density varied from 10^{12} to 10^{22} cm^{-3} . We note that this large span of carrier densities is not realistic for real materials, which for narrow gap semiconductors often have a lower bound determined by the intrinsic carrier density, and an upper bound set by its solubility limit. We nonetheless use this broad range to illustrate the expected trends when the carrier density is varied across material classes ranging from insulators to metals. When the highest carrier densities are used in the four geometries, we observe the common feature of a very low device resistance that is only weakly dependent on the magnetic field. In this case, the conductivity of the semiconductor is similar to or even exceeds that of the metal, and as the conductivity contrast across the metal/semiconductor interface becomes small, its capability to deflect the current path in magnetic fields vanishes [13]. Hence, the EMR effect is suppressed for all geometries. As the carrier density is lowered, we observe a gradual increase in the device resistance at all magnetic fields as well as the emergence of a pronounced field dependence of the resistance. At low carrier densities, the resistance follows a $R \propto 1/n$ behavior (see figure 3(m) for $B = 10 \text{ mT}$), suggesting that the device resistance is at this point dominated by the material properties of the semiconductor. A seemingly counter-intuitive feature

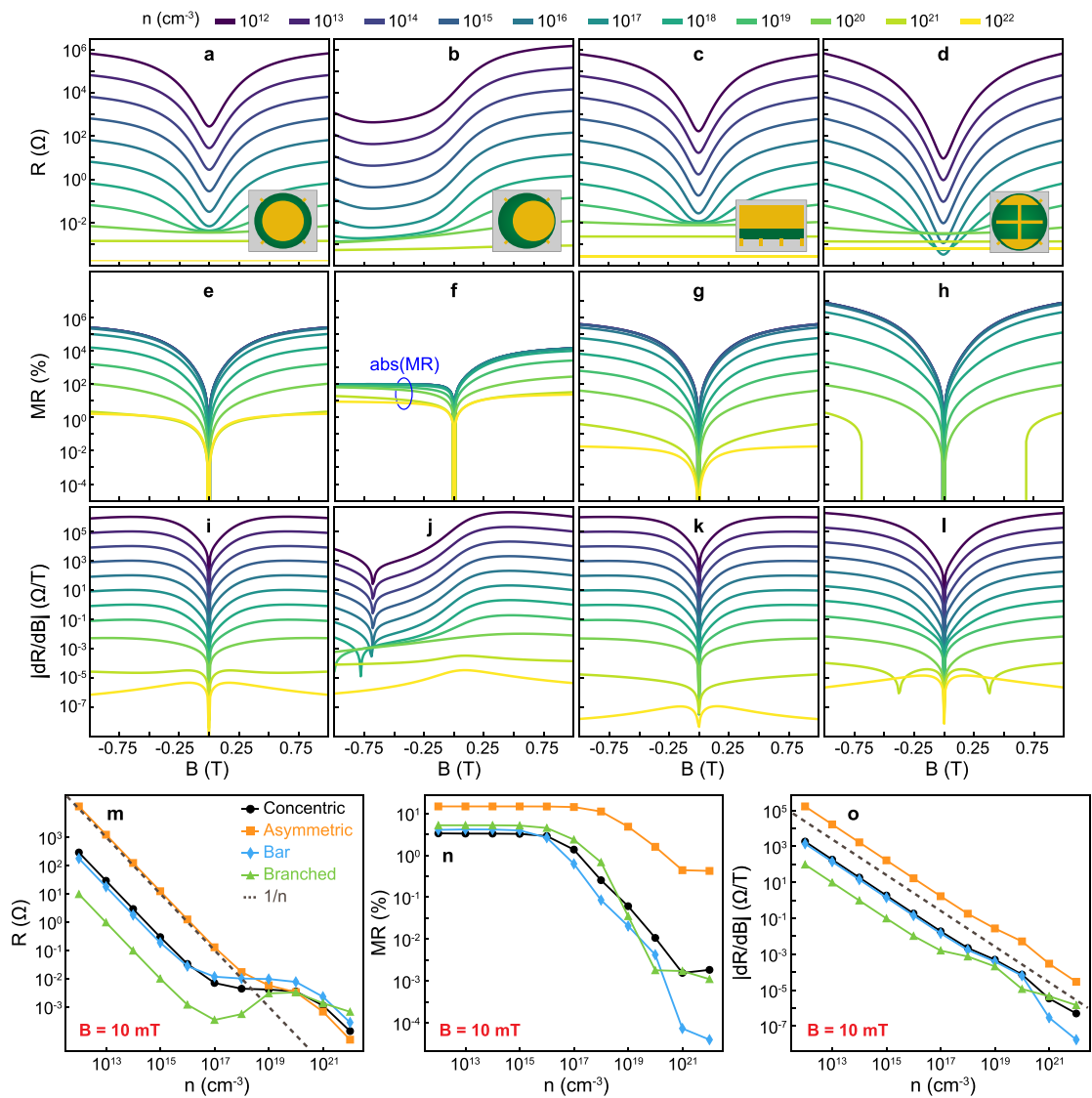


Figure 3. Carrier density variations showing the four-terminal resistance in (a)–(d), magnetoresistance in (e)–(h) and sensitivity in (i)–(l) as a function of magnetic field for the four different device geometries. (m)–(o): Shows the four-terminal resistance, magnetoresistance and sensitivity at $B = 10$ mT as a function of carrier density for the four different geometries.

observed in the branched device is that the resistance at a carrier density of 10^{17} cm^{-3} is lower than that obtained with a higher carrier density of 10^{20} cm^{-3} (figures 3(d) and (m)). We find this to be an effect of evaluating the resistance in a four-terminal configuration, as the corresponding two-terminal resistance drops monotonically as the carrier density is increased.

The emergence of a field-dependent resistance is readily observed in the magnetoresistance presented in figures 3(e)–(h). Here, a transition from a low to high MR is observed as the carrier density is decreased. This scenario was addressed in a previous study on the concentric circular geometry where it was concluded that the ratio of the conductivities of the metal and semiconductor should be higher than 500 in order to observe a large EMR effect [13]. This is consistent with all device studies here where the limit corresponds to a carrier density of $1.2 \cdot 10^{17} \text{ cm}^{-3}$ (see figure 3(n)). Decreasing the carrier density also increases the magnetoresistance, although the magnitude of the improvement saturates below around 10^{15} cm^{-3} ($\sigma_m/\sigma_s \approx 62000$) for all geometries except the asymmetric device which saturates below 10^{17} cm^{-3} (see figure 3(m)). In all cases, the high-field MR saturates at large values, ranging from 15 000% at $B = 1$ T for the asymmetric device to $7 \cdot 10^6\%$ for the branched structure (figures 3(e)–(h)). Here, the bar-shaped device and concentric circular device produce very similar magnetoresistances. As apparent from figures 3(a)–(d), the large spread in $\text{MR}(1 \text{ T})$ is primarily due to a lowering of $R(0 \text{ T})$ rather than an increase in $R(1 \text{ T})$. Here, the lowering of $R(0 \text{ T})$ is due to the different geometry of the metal region, leading to a small voltage drop and hence a small resistance for the branched structure where the gold inclusion efficiently bridges the source and drain

contact. In addition, the narrow semiconductor region between the voltage probes also leads to a small voltage drop for $B = 0$ and a large voltage drop for $B = 1$ T.

In contrast to the high-field case, the device with the highest MR at a magnetic field of 10 mT is the asymmetric device. This is independent of the carrier density as displayed in figure 3(n). For cases involving devices that are symmetric about their vertical axis, $R(B) = R(-B)$ and thus $dR/dB = 0$ for $B = 0$ T. Therefore, the magnetoresistance is positive for both positive and negative magnetic fields and builds up slowly at low magnetic fields. By breaking the mirror symmetry in the device, $dR/dB > 0$ for $B = 0$ T as shown previously [41], which produces a larger MR(10 mT), a negative MR for $B < 0$ T and a positive MR for $B > 0$ T. We here display the negative MR as the corresponding absolute values to conveniently show it on the same logarithmic plot (figure 3(f)).

The finite slope in the resistance curves of asymmetric devices at $B = 0$ also entails a large weak-field sensitivity as displayed in figures 3(i)–(l) and (o). High sensitivity is particularly interesting for magnetometry applications where $I \cdot dR/dB \cdot \Delta B$ gives the voltage signal when sensing a small field of ΔB with a constant bias current I . Interestingly, the sensitivity decreases as the carrier density is increased as $dR/dB \propto 1/n$ for all geometries, suggesting a boost of the sensor signal at low carrier densities. We also studied the effect of sheet carrier density (n_s) by fixing the 3d carrier density (n) and varying the thickness (t) of the device, and found that $dR/dB \propto 1/t$ whereas the magnetoresistance is thickness independent as expected (see figure S1 in the supplementary material). High sensitivity can therefore be obtained by lowering the sheet carrier density as $dR/dB \propto 1/n_s = 1/(nt)$. This optimization is similar to the case of Hall-bars featuring $dR_{xy}/dB \propto 1/n_s$. In both the case of Hall-bars and EMR devices, the signal strength for a fixed bias current increases faster than the thermal noise ($V_{\text{thermal}} \propto 1/\sqrt{n_s}$) as the sheet carrier density is decreased. This motivates the use of materials such as graphene and semiconductor 2-dimensional electron gases with low sheet carrier densities as the best-performing Hall and EMR sensors operating under fixed current bias. This is in contrast to previous studies which conclude that the signal-to-noise ratio scales as \sqrt{n} in the thermal noise limited regime [32]. The discrepancy is caused by the authors not taking into account the inverse dependence of the sensitivity on the sheet carrier density found here.

In a few cases as seen, e.g. for the asymmetric device at around $B = -0.7$ T, the device resistance has an inflection point leading to $dR/dB = 0$, which makes the EMR sensors incapable of working as magnetometers within this particular range of magnetic fields. These points are manifested as sharp dips in figures 3(j) and (l), which do not reach zero in our simulations due to the finite step size of 10 mT when sweeping the magnetic field. For all four EMR devices the optimal sensitivity is found at finite magnetic fields, which enables magnetometry for high-field applications. Further investigations on asymmetric devices with low carrier densities may have the potential of shifting the optimal measurement field close to $B = 0$ T. Decreasing the carrier density in the semiconductor further increases the conductivity ratio and enables the use of a lower conducting and potentially less expensive metal than gold without degrading the magnetoresistance of the device [10, 13, 33].

3.2. Carrier mobility

Varying the mobility of the semiconductor between 500 and $10^7 \text{ cm}^2 \text{ Vs}^{-1}$ dramatically affects the EMR response in all devices as shown in figure 4. The highest mobility was chosen to be $10^7 \text{ cm}^2 \text{ Vs}^{-1}$ which represents the high mobility of $3.5 \cdot 10^7 \text{ cm}^2 \text{ Vs}^{-1}$ observed in AlGaAs/GaAs heterostructures at cryogenic temperatures [45]. For mobilities above $10^7 \text{ cm}^2 \text{ Vs}^{-1}$, the conductivity of the semiconductor is within one order of magnitude of the metal, and above $10^8 \text{ cm}^2 \text{ Vs}^{-1}$ the conductivity of the semiconductor exceeds that of the metal. At mobilities equal to or lower than $1000 \text{ cm}^2 \text{ Vs}^{-1}$, the device resistances in all four cases show a weak field dependence in the range of $-1 \text{ T} < B < 1 \text{ T}$ (figures 4(a)–(d)) with the asymmetric case yielding the largest field dependence. As the mobility is increased from 1000 to $500\,000 \text{ cm}^2 \text{ Vs}^{-1}$, the zero field resistance initially decreases significantly and a pronounced field dependence appears. For the symmetric devices, the field dependence follows a parabolic-like behavior that sharpens as the mobility increases. For the asymmetric device, the field-dependent resistance for various mobilities also follows the general trend of shifting features to lower magnetic fields as the mobility increases, thus resulting in an overall sharper field dependence (figure 4(b)). Due to the asymmetric $R(B)$ curves, the field-dependent resistance appears more complex, but also provides a way to probe the direction of the magnetic field. Previous studies found that appreciable EMR effects require a mobility above $20\,000 \text{ cm}^2 \text{ Vs}^{-1}$ [18], which conforms well with our findings on all geometries. From $500\,000 \text{ cm}^2 \text{ Vs}^{-1}$ a second feature emerges characterized by a second increase in the resistance around 0.5 T , which shifts to lower magnetic fields as the mobility increases. It should, however, be noted that Shubnikov de Haas oscillations and—depending on device size—potentially ballistic effects will emerge at such high mobilities, both of which are not included in our diffusive model. Within the diffusive model presented here, the drop in the zero-field resistance saturates for $\mu \geq 500\,000 \text{ cm}^2 \text{ Vs}^{-1}$ which suggests that the resistivity of the metal starts to become a significant

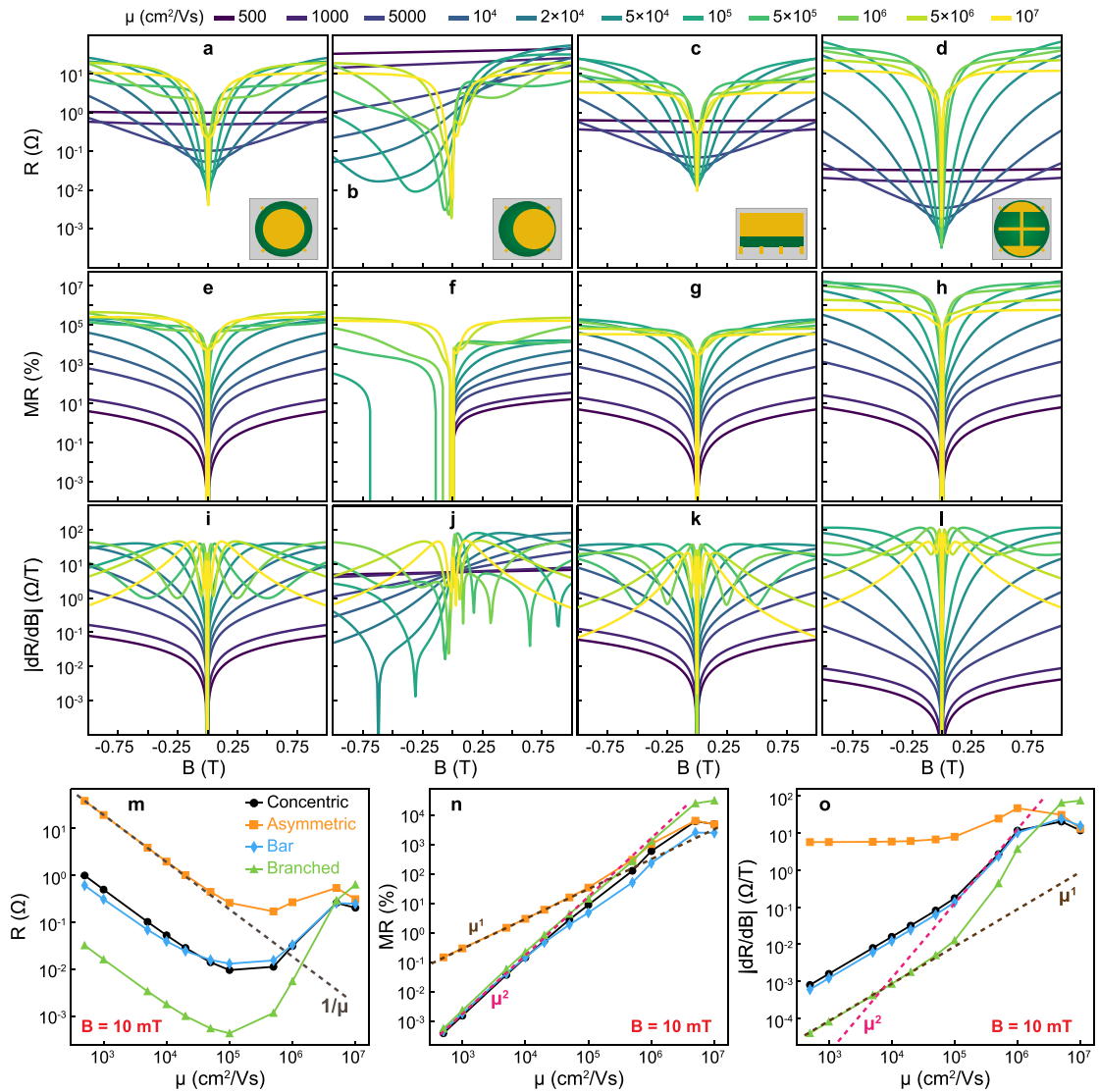


Figure 4. Variations in the electron mobility (μ) showing the four-terminal device resistance in (a)–(d), magnetoresistance in (e)–(h) and sensitivity in (i)–(l) as a function of magnetic field for the four different device geometries. (m)–(o) Shows the four-terminal resistance, magnetoresistance and sensitivity at $B = 10$ mT as a function of electron mobility for the four different geometries.

contribution to the hybrid device resistance. Within this same region of carrier mobility values, the low-field ($B = 10$ mT) resistance increases as a result of the shift in the location of the features towards lower magnetic fields with increasing mobility (see figure 4(m)).

Further increasing the mobility up to $5 \cdot 10^6$ cm² Vs^{−1} leads to higher MR values with a sharper response. The magnetoresistance of the bar and branched structures reaches a peak value at mobilities of 200 000% and $1.6 \cdot 10^7$ %, respectively. The EMR effect saturates when all current is being deflected away from the metallic inclusion, which occurs when the Hall angle approaches 90°. A higher mobility produces a larger Hall angle for a given magnetic field, which results in a stronger current deflection and a saturation of the magnetoresistance at lower magnetic fields. Interestingly, the optimal mobility value seems to differ between geometries. For the concentric circular geometry, the highest MR at 1 T can be obtained when the carrier mobility is between 10^6 and $5 \cdot 10^6$ cm² Vs^{−1}, and for the asymmetric device the optimal mobility is $5 \cdot 10^6$ cm² Vs^{−1}. For the bar and branched structures, the optimal mobilities are 100 000 cm² Vs^{−1} and between 100 000–500 000 cm² Vs^{−1}, respectively. The branched structure showed the highest magnetoresistance and with a carrier mobility of only 20 000 cm² Vs^{−1} was able to outperform all of the other geometries across the entire range of mobility values.

The resistance of all devices at weak fields ($B = 10$ mT) roughly scales as μ^{-1} up to around 100 000 cm² Vs^{−1} as the transport in this regime is dominated by the properties of the semiconductor (see figure 4(m)). Using a conductivity ratio of ~ 500 between the metal and semiconductor as described above, we obtain a semiconductor mobility of 224 000 cm² Vs^{−1} which is consistent with the change in behavior

occurring around this value. Interestingly, the weak-field magnetoresistance increases roughly quadratically with the mobility for all symmetric devices, whereas the magnetoresistance of the asymmetric device increases linearly (see figure 4(n)). This along with the general trend of shifting the features to lower magnetic fields as the mobility is increased motivate a rescaling of the magnetoresistance as a function of μB (see figure S2 in the supplementary material). Here, it is generally observed that the field-dependent magnetoresistances collapse onto two curves scaling either as μB or $(\mu B)^2$. The asymmetric device generally shows a μB scaling whereas the symmetric devices predominantly show a $(\mu B)^2$ behavior, however, the symmetric devices exhibit a transition from one scaling to another. This is in reasonable agreement with previous studies which describe how the magnetoresistance is comprised of both symmetric and asymmetric contributions: $MR = G_{as}\mu B + G_s(\mu B)^2$ where G_{as} and G_s are asymmetric and symmetric geometric factors, respectively [46]. The scaling has an origin in the factor of μB present in the off-diagonal component of the conductivity tensor.

The traces of the EMR sensitivity also shift to lower magnetic fields as the mobility is increased for all geometries (figures 4(i)–(l)), consistent with the study of [13] for the case of the concentric circular device and [33] for the bar-shaped device. Interestingly, the peak value of the sensitivity remains at the same magnitude for each device independent of the mobility, but varying the mobility determines the magnetic field where the EMR sensor is most sensitive. Hence, higher mobility values shift the peak sensitivity of the EMR devices to lower magnetic fields. The sensitivity peak reaches a maximum value of 41 and 121 ΩT^{-1} for the bar-shaped and branched devices, respectively. For comparison, a Hall-bar composed of the same semiconducting material with a thickness of 1.3 μm would show a mobility-independent Hall resistance of $dR_{xy}/dB = 192 \Omega T^{-1}$. The weak-field sensitivity initially increases linearly with the mobility for the symmetric devices, which is succeeded by, firstly, a superlinear regime above 100 000 $cm^2 Vs^{-1}$ and, secondly, a saturated regime when the mobility exceeds a 1000 000 $cm^2 Vs^{-1}$ (figure 4(o)). In contrast, the sensitivity of the asymmetric device is initially independent of the mobility up to a value of around 100 000 $cm^2 Vs^{-1}$. For the symmetric devices, the weak-field sensitivity and conductivity thus both increase when highly mobile semiconductors are used, which translates to higher signal strength and lower noise when measuring weak fields, respectively. The field-dependent sensitivities for various mobility values also collapse onto a single curve when plotted as a function of μB (figures S2(e)–(h)). Here, the sensitivity transitions from a μB to $(\mu B)^2$ for the symmetric devices. In contrast, the asymmetric device is independent of μB at values below 0.1 and partially transitions into a μB scaling above this value.

3.3. Contact resistance

Figure 5 shows how varying the interface resistance, ρ_c , between the metal inclusion and the semiconductor region affects the four EMR geometries. The contact resistance is assumed to be Ohmic and varied between 10^{-8} and $10 \Omega cm^2$, with experimental EMR devices featuring, e.g. a contact resistance of $7 \cdot 10^{-8} \Omega cm^2$ for the InAs/Au device [47] and $3.7 \cdot 10^{-6} \Omega cm^2$ for a graphene/Au EMR device [27]. When normalized with the interface area between the metal and semiconductor, the Sharvin resistance has been used to theoretically predict a lower limit for the contact resistance on the order of $1 \cdot 10^{-8} \Omega cm^2$ [47, 48]. We note that EMR devices with nonlinear contacts may result in different current deflections and EMR behavior compared to the one calculated here as both the direction and magnitude of the local current density varies greatly along the metal/semiconductor boundary in an EMR device.

All geometries suffer from a field-independent resistance when the contact resistance is large (figures 5(a)–(d)). This behavior has been previously discussed [10, 13], and it arises as the EMR effect diminishes when the gold inclusion becomes inactive due to the highly resistive contact barrier. By gradually lowering the contact resistance, the field-dependent resistance as well as the magnetoresistance emerge and eventually saturate (figures 5(a)–(h)). All four geometries exhibit large MR responses at 1 T when $\rho_c \leq 10^{-4} \Omega cm^2$. The sensitivity is also strongly affected by the contact resistance with the overall trend suggesting that low contact resistances are generally needed to achieve high sensitivities for most magnetic field values (figures 5(i)–(l)). A few notable exceptions exist such as for $-1 T < B < 0 T$ in the case of the asymmetric device where decoupling the shunt using a high contact resistance exceeding $0.1 \Omega cm^2$ yields a higher sensitivity than the lowest modeled contact resistance (figure 5(j)).

The resistance and magnetoresistance responses evaluated at a small field of 10 mT follow clear trends where lower contact resistances monotonically decrease the total resistance and increase the magnetoresistance until saturation is reached (figures 5(m)–(n)). For all geometries, the saturation occurs approximately below $1 \cdot 10^{-5} \Omega cm^2$ except for the bar-shaped device where the saturation only occurs below $1 \cdot 10^{-7} \Omega cm^2$. The effect of the contact resistance on the sensitivity evaluated at 10 mT and 0 T is depicted in figures 5(o) and S3, respectively. We observed only small variations in the sensitivity of the asymmetric device as the contact resistance was increased, however, the overall sensitivity value was high and consistent with previous studies [41]. For particular the bar-shaped and branched devices, the weak-field sensitivity is

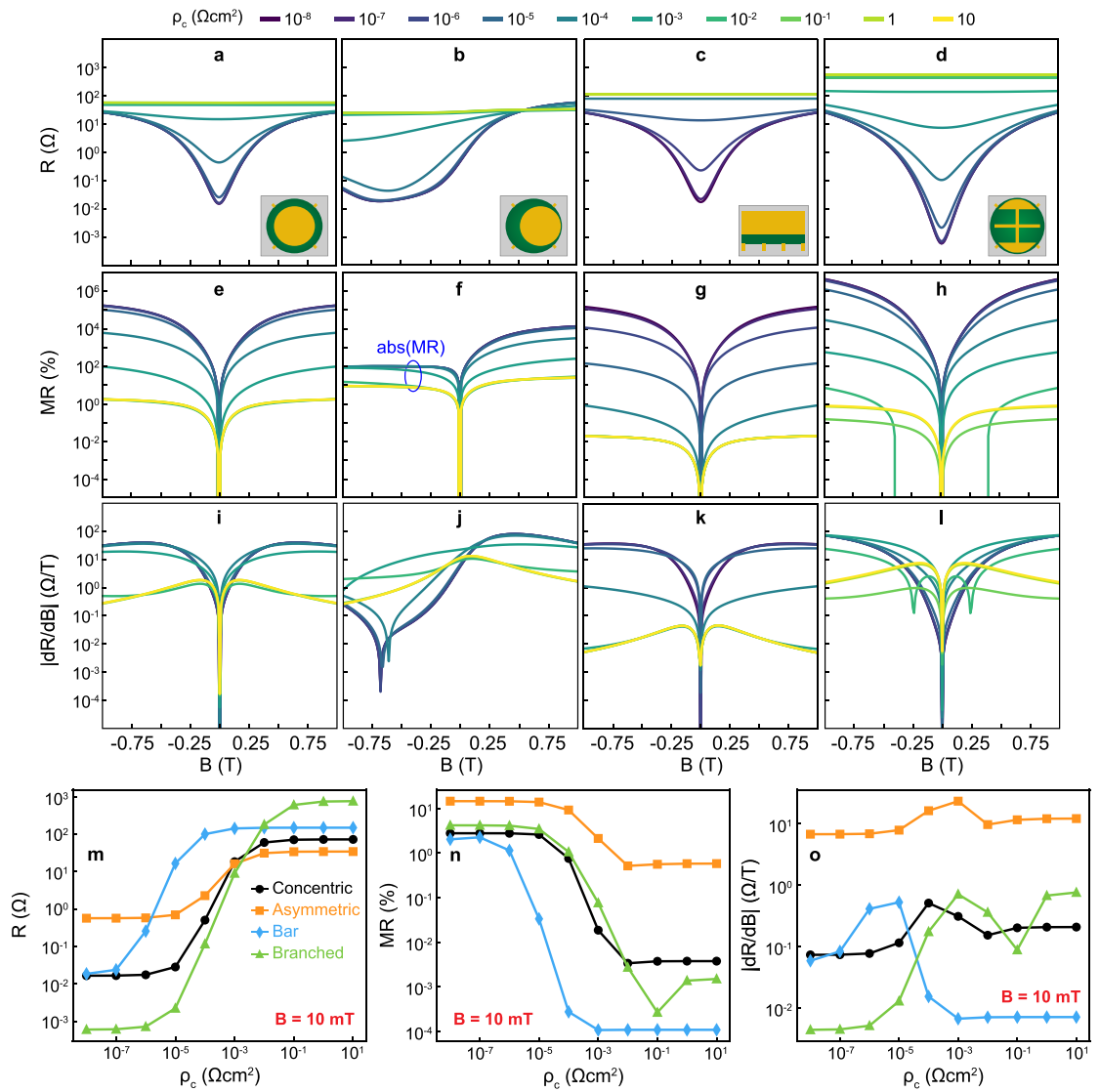


Figure 5. Contact resistance variations showing the four-terminal resistance in (a)–(d), magnetoresistance in (e)–(h) and sensitivity in (i)–(l) as a function of magnetic field for the four different device geometries. (m)–(o) Shows the four-terminal resistance, magnetoresistance and sensitivity at $B = 10$ mT as a function of contact resistance for the four different geometries.

observed to have a non-monotonic dependence on the contact resistance, which arises from the complexity in figures 5(k)–(l). In contrast, evaluating the sensitivity at 1 T shows a clear trend where the sensitivity saturates below $1 \cdot 10^{-3} \Omega\text{cm}^2$ for all devices except for the bar-shaped device where saturation occurs below $1 \cdot 10^{-5} \Omega\text{cm}^2$ (figure S4). Raising the contact resistance significantly above these threshold values results in a drastic drop in the sensitivity at $B = 1$ T. For all four devices, these threshold values are around two orders of magnitude larger than the corresponding threshold values where the magnetoresistance at 1 T drops significantly (figure S4). This suggests that for all geometries the sensitivity is more robust towards poor electrical contact as also observed for the bar-shaped geometry [12].

4. Promising materials

The key criteria for selecting materials compatible with a high magnetoresistance are high mobility, low contact resistance, and a significant contrast in the conductivity of the constituent materials. To evaluate how different combinations of material properties affect the performance of EMR sensors we model the expected MR of devices made from several high-mobility materials from various material classes, including 2D materials (graphene encapsulated in hexagonal boron nitride), III–V semiconductors (InSb and AlGaAs/GaAs) as well as oxides (MgZnO/ZnO, SrTiO₃, and γ -Al₂O₃/SrTiO₃). For simplicity, all materials are interfaced with gold assuming no contact resistance, no sticking layer, and fully diffusive transport. Experimental realization of a neglectable contact resistance is problematic for material platforms such as

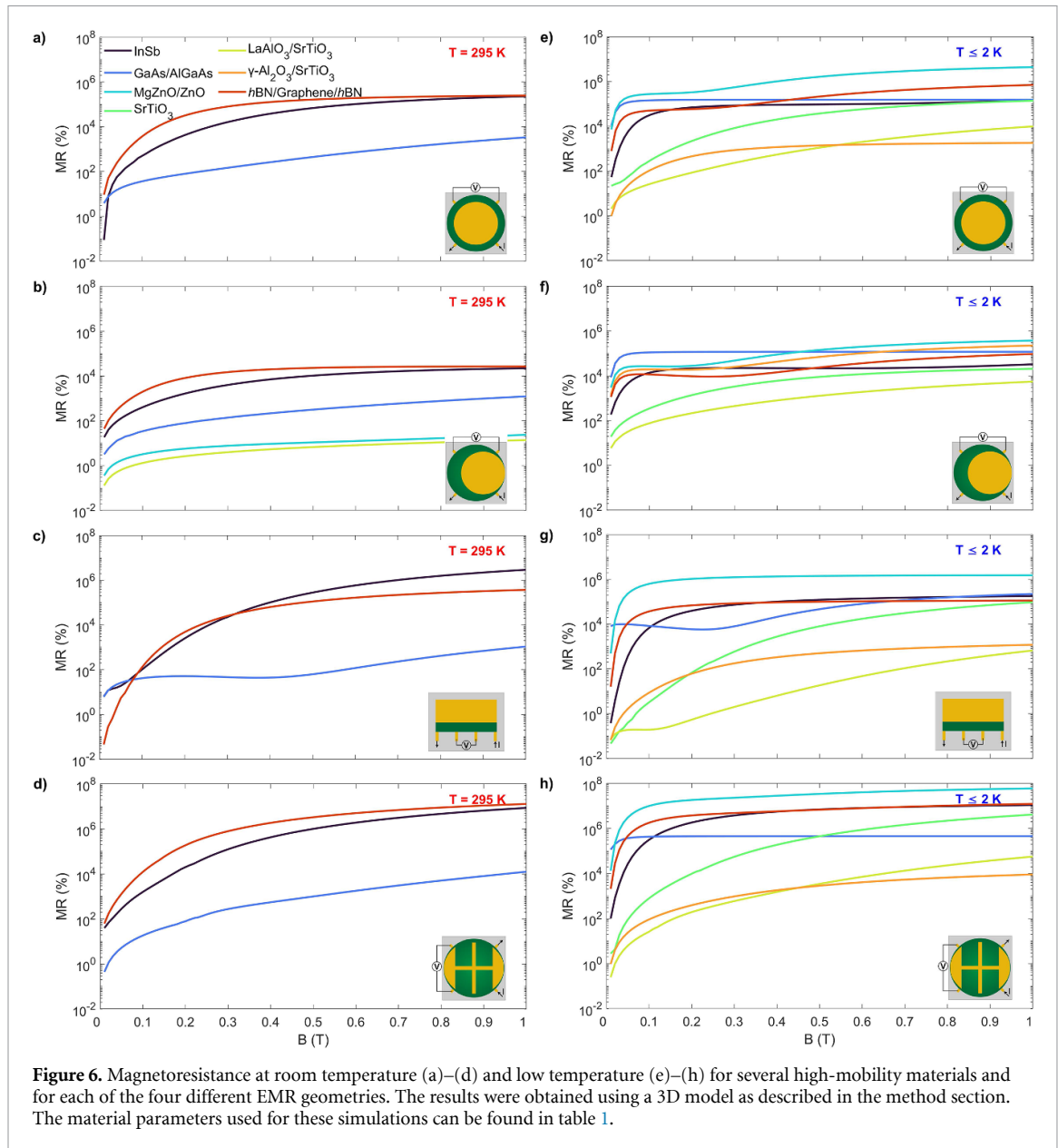
Table 1. table of material parameters used in figure 6.

Material	Dim.	Temperature (K)	Mobility ($\text{cm}^2 (\text{Vs}^{-1})$)	Carrier Density (cm^{-3}) or (cm^{-2})	Thickness (nm)	References
InSb	3D	295	45 500	$2.5 \cdot 10^{16} \text{ cm}^{-3}$	1300	[8]
	2D	2	324 000	$1.5 \cdot 10^{12} \text{ cm}^{-2}$	30	[49]
GaAs/AlGaAs	2D	295	7900	$5.4 \cdot 10^{11} \text{ cm}^{-2}$	13	[50]
	2D	0.36	$3.5 \cdot 10^7$	$3.0 \cdot 10^{11} \text{ cm}^{-2}$	13	[45]
MgZnO/ZnO	2D	295	440	$1.0 \cdot 10^{16} \text{ cm}^{-3}$	15	[51, 52]
	3D	0.1	$1.2 \cdot 10^6$	$6.0 \cdot 10^{10} \text{ cm}^{-2}$	15	[53]
SrTiO ₃	3D	295	6	$8.0 \cdot 10^{18} \text{ cm}^{-3}$	60	[54]
	3D	1.8	42 000	$3.0 \cdot 10^{17} \text{ cm}^{-3}$	60	[55]
LaAlO ₃ /SrTiO ₃	2D	295	350	$8.7 \cdot 10^{13} \text{ cm}^{-2}$	7	[56, 57]
	2D	2	18 000	$2.5 \cdot 10^{13} \text{ cm}^{-2}$	7	[56, 57]
γ -Al ₂ O ₃ /SrTiO ₃	2D	295	12	$2.0 \cdot 10^{14} \text{ cm}^{-2}$	0.9	[58, 59]
	2D	2	140 000	$3.0 \cdot 10^{14} \text{ cm}^{-2}$	8	[58, 59]
hBN/Graphene/hBN	2D	295	100 000	$1.0 \cdot 10^{12} \text{ cm}^{-2}$	0.34	[60, 61]
	2D	1.7	$1.0 \cdot 10^6$	$1.0 \cdot 10^{12} \text{ cm}^{-2}$	0.34	[61]

GaAs/AlGaAs quantum wells, yet it is excluded here for simplicity. The results thus effectively represent an upper bound for the magnetoresistance with the actual performance depending on the quality of the contact resistance as discussed in the previous section.

It should be noted that the material properties we selected are not representative of typical samples, but rather represent some of the highest reported values within the various material classes (see table 1). For 2-dimensional electron gases confined in quantum wells, the sheet carrier density is converted to a 3-dimensional carrier density using the reported effective thicknesses given in the table, however, the thickness of these quantum wells may contain significant uncertainties in cases such as γ -Al₂O₃/SrTiO₃ [62]. By applying the 2D model to high-mobility graphene, we find a relatively low magnetoresistance, which contrasts experiments [30]. This is caused by the 2D model assuming the same thickness for both the gold and graphene, and as the conductivities of high-mobility graphene and gold are similar, the 2D model predicts a low performance consistent with figure 3. In actual devices, however, a metal with a thickness of several tens of nanometers is contacted to the atomically thin graphene sheet, which is only 0.34 nm thick. Therefore, we model 2-dimensional electron gases using a 3D model (see methods), which takes into account the different thicknesses of the constituent materials from table 1, using a fixed gold thickness of 60 nm and the material data provided in table 1 for the 2-dimensional electron gases. We stress that only in this case of 2D gases, the metal thickness is taken to be different from that of the semiconductor.

We show both low and room temperature simulations for the four different device geometries using the various material platforms (see figure 6). At room temperature, we observe that graphene and InSb both produce a large MR in all four EMR geometries owing to their high room-temperature mobility and significant conductance contrast to the metal (see figures 6(a)–(d)). This trend is consistent with the largest MR values being observed in graphene encapsulated with hexagonal boron nitride ($\sim 10^7\%$ at 9 T) [30] and InSb ($\sim 1 \cdot 10^6\%$ at 5 T) [8], both in concentric circular geometries. At 1 T, the best experimental results from the encapsulated graphene device with $\alpha = 12/16$ showed an MR of approximately $5 \cdot 10^4\%$, which is lower than the model estimate ($2 \cdot 10^5\%$) with the same filling factor by a factor of 4. It should be noted that the experimental data was obtained using electrostatic gating which significantly changes the material properties and that signs of ballistic transport were observed [30], neither of which are not taken into account in our model. For InSb, an experimental device exhibited an MR response of $1.5 \cdot 10^5\%$ at 1 T for the concentric circular device with $\alpha = 12/16$ [8], which is in good agreement with the value of $2.4 \cdot 10^5\%$ obtained here. Interestingly, only for the bar-shaped device is graphene outperformed by InSb in the range $B = 0$ –0.1 T and $B > 0.3$ T. We further predict that the magnetoresistance at room temperature can be increased by around two orders of magnitude if the branched geometry is used. For the other materials modeled here, particularly the oxides, the magnetoresistance at room temperature is much lower due to their low room-temperature mobility. MgZnO/ZnO only produces a visible magnetoresistance signal in the asymmetric device in the modeled field range, reinforcing the importance of the asymmetric geometry in the case of a moderate mobility.



For low temperatures, the highest magnetoconductance is obtained using MgZnO/ZnO owing to an appealing combination of very high electron mobility and low carrier density. The highest magnetoconductance was found using MgZnO/ZnO shaped in a branched geometry, yielding a value of almost $10^8\%$ at 1 T. MgZnO/ZnO was only outclassed in a single geometry (the asymmetric device) by the AlGaAs/GaAs heterostructure with a record-high mobility of $3.5 \cdot 10^7 \text{ cm}^2 \text{ Vs}^{-1}$. The generally lower magnetoconductance of AlGaAs/GaAs despite its higher mobility is caused by the larger conductivity, which lowers the conductivity contrast between the metal and semiconductor. At low fields, however, the MR quickly reaches a high value as observed, e.g. in the branched geometry (figure 6(d)). Lowering the temperature also results in all modeled high-mobility materials showing a sizable magnetoconductance exceeding 1000% at 1 T for the four geometries shown here, and even consistently above 10 000% for the branched structure. A very high magnetoconductance is therefore expected to be obtainable across several distinct material classes. Options for improving the magnetoconductance of the two-dimensional electron gases beyond the values reported here include the optimization of the geometry and the material properties using, e.g. electrostatic gating and increasing metal sheet conductance, whereas a finite contact resistance may lower the performance.

5. Discussion and outlook

Overall, a range of universal trends and differences are observed when comparing material variations across the four very distinct EMR geometries. We here summarize the key trends in terms of achieving high

magnetoresistance and high sensitivity and provide a perspective of these findings for the use in magnetic field sensors:

1. **Magnetoresistance:** At very large carrier densities, the four geometries all display a low device resistance which is only weakly dependent on the magnetic field as a result of poor conductivity contrast between the metal and semiconductor. When lowering the carrier density below $n = 10^{18} \text{ cm}^{-3}$, the resistance follows a $R \propto 1/n$ behavior as the material properties of the semiconductor start to dominate the device resistance. Here, a pronounced magnetoresistance also emerges, which saturates in all devices at a carrier density of $n = 10^{16} \text{ cm}^{-3}$ or lower. The lowest saturation value of 15 000% at 1 T is found for the asymmetric device whereas the highest value forms in the branched geometry producing $\text{MR} = 7 \cdot 10^6\%$ at 1 T. However, at a low magnetic field (10 mT) the asymmetric design yields the highest MR. Varying the mobility revealed that an appreciable magnetoresistance for $B < 1 \text{ T}$ requires a mobility exceeding approximately $20\,000 \text{ cm}^2 \text{ Vs}^{-1}$ in all devices. For lower values, all four geometries showed a weak field dependence with the asymmetric device performing slightly better. Increasing the mobility up to $500\,000 \text{ cm}^2 \text{ Vs}^{-1}$, resulted in a significant decrease of the zero field resistance and an emergence of a pronounced magnetoresistance. The increase in the mobility shifts the features to lower magnetic fields, effectively sharpening the magnetoresistance response. A high contact resistance destroys the EMR as the gold inclusion becomes inactive. The general trend is that a contact resistance below approximately $\rho_c = 10^{-4} \Omega \text{ cm}^2$ is required for achieving the highest magnetoresistance, but no further gain in magnetoresistance is observed below approximately $\rho_c = 10^{-5} \Omega \text{ cm}^2$ (see figure S4 in the supplementary material).

From the modeled high-mobility materials, both graphene encapsulated in hexagonal boron nitride and InSb are promising materials for obtaining high magnetoresistance at room temperature for all devices. The largest value exceeding $10^7\%$ at 1 T was observed for encapsulated graphene devices with a branched gold inclusion. For low temperatures, all modeled materials and device geometries produced a sizeable magnetoresistance. MgZnO/ZnO, encapsulated graphene, and InSb stand out as particularly suitable materials for achieving a high magnetoresistance. The best performing device in our study was that of the MgZnO/ZnO heterostructure in a branched geometry at low temperature, which showed a magnetoresistance of almost $10^8\%$ at 1 T.

2. **Sensitivity:** Lowering the carrier density resulted in an increase in dR/dB which was inversely proportional to the sheet carrier density of the semiconductor for all four geometries. This emphasizes the importance of lowering the 3D carrier density as well as the thickness of the conducting layer for achieving high sensitivity. With these considerations in mind, encapsulated graphene is a natural candidate as it is atomically thin and can exhibit extremely low sheet carrier densities on the order of 10^9 cm^{-2} through the use of an applied gate voltage [63]. Both quadratic and linear scaling of the low-field sensitivity was observed when the carrier mobility was varied with the highest sensitivity obtained for high mobilities in both cases. The asymmetric device is clearly the preferred choice for the very weak magnetic fields owing to the asymmetric $R(B)$ curves and non-zero sensitivity at $B = 0 \text{ T}$ (see figure S3 in the supplementary material). However, the branched structure showed a higher peak sensitivity of $70 \Omega/\text{T}$ at 10 mT for the highest mobility values while also excelling at higher magnetic fields. A complex weak-field behavior of the sensitivity was observed in most geometries when varying the contact resistance. In contrast, if the magnetic field is increased to 1 T, the sensitivity increases monotonously as the contact resistance is lowered until saturation is reached for contact resistances at $\rho_c \leq 1 \cdot 10^{-5} \Omega \text{ cm}^2$ for the bar-shaped geometry and $\rho_c \leq 1 \cdot 10^{-3} \Omega \text{ cm}^2$ for the remaining device geometries (see figure S4).
3. **Magnetic field sensors:** When aiming to use EMR devices as magnetometers, the appropriate figure of merit is the noise-equivalent field [19, 32], which describes the detection limit defined as the magnetic field resulting in a signal-to-noise ratio of 1. If the EMR sensor is limited by thermal noise and operated at a constant current, the noise-equivalent field (B_{NEF}) when measuring small magnetic field signals in a background or bias magnetic field (B_b) is:

$$B_{\text{NEF}} = \frac{\sqrt{4k_B T R_{V,2T}(B_b)}}{I \frac{dR}{dB} \big|_{B_b}} \quad (5)$$

where $R_{V,2T}$ is the two-terminal resistance between the voltage probes and R is the four-terminal resistance. If we consider the range of mobilities and carrier densities that produce a sizeable EMR effect, the resistance is dominated by the semiconductor material properties and $R_{V,2T} \propto 1/(n_s \mu)$. In addition, we found here that $dR/dB \propto 1/n_s$ and $dR/dB \propto \mu^m$ with $m \geq 0$ for $B = 10 \text{ mT}$. Hence, for a fixed current we obtain $B_{\text{NEF}} \propto \sqrt{n_s}$ and $B_{\text{NEF}} \propto 1/(\mu^{0.5+m})$. This motivates the use of a material with a low sheet

carrier density and high mobility to achieve the lowest detection limit for a fixed current. We caution that relaxing the assumption of a fixed current and instead treating the current as an optimization parameter may alter these target material properties. Nonetheless, in circumstances where this is not the case, the target material properties at room temperature point towards using encapsulated graphene gated close to the charge neutrality point as the optimal material. However, in this regime graphene may have complex transport mechanisms, spatially inhomogeneous conductivity, as well as displaying ballistic and other quantum effects. These effects are not included in the present diffusive model and further numerical modeling may be needed to elucidate this regime. In addition, a complete diffusive investigation of universal trends for achieving the best noise-equivalent field with various noise contributions and under consideration of the optimal bias current is also of high interest for future studies of designing optimized EMR sensors.

In conclusion, we have investigated how variations in semiconductor carrier density, mobility, and interface contact resistance have affected four EMR geometries: the concentric circular device, an asymmetric circular device, the bar-shaped device, and an optimized multi-branched device. The results in this study allowed the extraction of several key trends across the four geometries, which provides universal insight into understanding how material parameters affect EMR performance. While this study provides the framework for material selection in EMR sensors, experimental confirmation is required to fully benefit from the results. In particular, our studies point to high-quality encapsulated graphene being a promising material for both low and room temperature operation, but especially when using high-mobility encapsulated graphene for making EMR devices with a size of a few micrometers or less, it remains unclear to which extent the present diffusive EMR model can describe the EMR transport behavior. Further studies should also include systematic studies on the noise-equivalent-field with different noise contributions and the inclusion of expressions for the optimal bias current. Interesting directions for expanding our study also include adding additional physical processes where, e.g. the non-magnetic materials are replaced with magnetic or superconducting materials to enrich the field-response via spin-dependent scattering processes and phase transitions. This may lead to a rich temperature dependence where the current deflection in the EMR device couples intimately to the transport in the magnetic or superconducting material, potentially leading to an enlargement of the negative magnetoresistance in asymmetric EMR devices comprising magnetic materials and a boost in the positive magnetoresistance in symmetric EMR comprising superconductors. Despite the need for future model extensions, our study presents a significant step towards providing universal guidelines for developing EMR magnetoresistive devices and magnetometers.

Data availability statement

All data that support the findings of this study are included within the article (and any supplementary files).

Acknowledgments

D V C, N P and R B acknowledge funding from the Novo Nordic Foundation, Grant No. NNF21OC0066526 (BioMag), and D V C further acknowledges support from the Novo Nordic Foundation Nerd program, Grant No. NNF21OC0068015 (Superior).

ORCID iDs

Ricci Erlandsen  <https://orcid.org/0000-0002-7115-0618>

Lior Kornblum  <https://orcid.org/0000-0001-6305-7619>

Nini Pryds  <https://orcid.org/0000-0002-5718-7924>

Rasmus Bjørk  <https://orcid.org/0000-0002-3728-2326>

Dennis V Christensen  <https://orcid.org/0000-0003-0048-7595>

References

- [1] Grochowski E and Halem R D 2003 Technological impact of magnetic hard disk drives on storage systems *IBM Syst. J.* **42** 338
- [2] Holz M, Kronenwerth O and Grundler D 2003 Optimization of semiconductor-metal hybrid structures for application in magnetic-field sensors and read heads *Appl. Phys. Lett.* **83** 3344
- [3] Solin S A 2006 Design and properties of a scanning EMR probe microscope (arXiv:cond-mat/0602146)
- [4] Kodama R H 1999 Magnetic nanoparticles *J. Magn. Magn. Mater.* **200** 359
- [5] Ito A, Shinkai M, Honda H and Kobayashi T 2005 Medical application of functionalized magnetic nanoparticles *J. Biosci. Bioeng.* **100** 1

- [6] Cardoso V F, Francesko A, Ribeiro C, Ba noble-López M, Martins P and Lanceros-Mendez S 2018 Advances in magnetic nanoparticles for biomedical applications *Adv. Healthcare Mater.* **7** 1700845
- [7] Campos F, Bonhome-Espinosa A B, Carmona R, Durán J D, Kuzhir P, Alaminos M, López-López M T, Rodriguez I A and Carriel V 2020 *In vivo* time-course biocompatibility assessment of biomagnetic nanoparticles-based biomaterials for tissue engineering applications *Mater. Sci. Eng. C* **118** 111476
- [8] Solin S A, Thio T, Hines D R and Heremans J J 2000 Enhanced room-temperature geometric magnetoresistance in inhomogeneous narrow-gap semiconductors *Science* **289** 1530
- [9] Moussa J, Ram-Mohan L R, Sullivan J, Zhou T, Hines D R and Solin S A 2001 Finite-element modeling of extraordinary magnetoresistance in thin film semiconductors with metallic inclusions *Phys. Rev. B* **64** 184410
- [10] Holz M, Kronenwerth O and Grundler D 2003 Magnetoresistance of semiconductor-metal hybrid structures: the effects of material parameters and contact resistance *Phys. Rev. B* **67** 195312
- [11] Sun J and Kosel J 2013 Extraordinary magnetoresistance in semiconductor/metal hybrids: a review *Materials* **6** 500
- [12] Sun J and Kosel J 2012 Finite element analysis on the influence of contact resistivity in an extraordinary magnetoresistance magnetic field micro sensor *J. Supercond. Nov. Magn.* **25** 2749
- [13] Hewett T and Kusmartsev F 2012 Extraordinary magnetoresistance: sensing the future *Open Phys.* **10** 602–8
- [14] Zhou T, Hines D R and Solin S A 2001 Extraordinary magnetoresistance in externally shunted van der Pauw plates *Appl. Phys. Lett.* **78** 667
- [15] Solin S, Hines D, Tsai J, Pashkin Y, Chung S, Goel N and Santos M 2002 Room temperature extraordinary magnetoresistance of nonmagnetic narrow-gap semiconductor/metal composites: application to read-head sensors for ultrahigh-density magnetic recording *IEEE Trans. Magn.* **38** 89
- [16] Sosa S S 2002 Extraordinary magnetoresistance of InSb allows fabrication of a read-head sensor without magnetic noise *MRS Bull.* **27** 494
- [17] Oszwaldowski M, El-Ahmar S and Jankowski J 2012 Extraordinary magnetoresistance in planar configuration *J. Phys. D: Appl. Phys.* **45** 145002
- [18] Holz M, Kronenwerth O and Grundler D 2003 Semiconductor-metal hybrid structures: novel perspective for read heads *Sensors* **4** 1245–8
- [19] Möller C H, Kronenwerth O, Heyn C and Grundler D 2004 Low-noise magnetic-flux sensors based on the extraordinary magnetoresistance effect *Appl. Phys. Lett.* **84** 3343
- [20] Hoener M, Kronenwerth O, Heyn C, Grundler D and Holz M 2006 Geometry-enhanced magnetoresistance of narrow Au/InAs hybrid structures incorporating a two-dimensional electron system *J. Appl. Phys.* **99** 036102
- [21] Wittmann A, Möller C-H, Kronenwerth O, Holz M and Grundler D 2004 Hybrid ferromagnet/semiconductor nanostructures: spin-valve effect and extraordinary magnetoresistance *J. Phys.: Condens. Matter* **16** S5645
- [22] Terra F S, Higazy A A, Mahmoud G M and Mansour A M 2010 (InSb/GaAs)-Au hybrid macro-structure prepared by flash evaporation *Indian J. Phys.* **84** 265
- [23] Wu D-C, Pan Y-W, Wu J-S, Lin S-W and Lin S-D 2016 High-sensitivity two-terminal magnetoresistance devices using InGaAs/AlGaAs two-dimensional channel on GaAs substrate *Appl. Phys. Lett.* **108** 172403
- [24] Wunderlich J, Jungwirth T, Novak V, Irvine A C, Kaestner B, Shick A B, Foxon C T, Campion R P, Williams D A and Gallagher B L 2007 Ordinary and extraordinary Coulomb blockade magnetoresistance in a (Ga,Mn)As single electron transistor *Solid State Commun.* **6** 536–541
- [25] Pisana S, Braganca P M, Marinero E E and Gurney B A 2010 Tunable nanoscale graphene magnetometers *Nano Lett.* **10** 341
- [26] Lu J, Zhang H, Shi W, Wang Z, Zheng Y, Zhang T, Wang N, Tang Z and Sheng P 2011 Graphene magnetoresistance device in van der Pauw geometry *Nano Lett.* **11** 2973
- [27] Pisana S, Braganca P M, Marinero E E and Gurney B A 2010 Graphene magnetic field sens. *IEEE Trans. Magn.* **46** 1910
- [28] Friedman A L, Robinson J T, Perkins F K and Campbell P M 2011 Extraordinary magnetoresistance in shunted chemical vapor deposition grown graphene devices *Appl. Phys. Lett.* **99** 022108
- [29] Moktadir Z and Mizuta H 2013 Magnetoresistance in inhomogeneous graphene/metal hybrids *J. Appl. Phys.* **113** 083907
- [30] Zhou B, Watanabe K, Taniguchi T and Henriksen E A 2020 Extraordinary magnetoresistance in encapsulated monolayer graphene devices *Appl. Phys. Lett.* **116** 053102
- [31] El-Ahmar S, Koczorowski W, Poźniak A, Kuświk P, Przychodnia M, Dembowski J and Strupiński W 2019 Planar configuration of extraordinary magnetoresistance for 2D-material-based magnetic field sensors *Sens. Actuators A* **296** 249
- [32] Shao Y, Solin S A, Ram-Mohan L R and Yoo K-H 2007 Optimizing the physical contribution to the sensitivity and signal to noise ratio of extraordinary magnetoresistance quantum well structures *J. Appl. Phys.* **101** 123704
- [33] Rong C-B, Zhang H-W, Sun J-R and Shen B-G 2006 Geometry and material optimization of the extraordinary magnetoresistance in the semiconductor-metal hybrid structure *J. Magn. Magn. Mater.* **301** 407
- [34] Holz M, Kronenwerth O and Grundler D 2004 Optimization of the extraordinary magnetoresistance in semiconductor-metal hybrid structures for magnetic-field sensor applications *Physica E* **21** 897
- [35] Sun J, Gooneratne C P and Kosel J 2012 Design study of a bar-type EMR device *IEEE Sens. J.* **12** 1356
- [36] Sun J, Soh Y-A and Kosel J 2013 Geometric factors in the magnetoresistance of n-doped InAs epilayers *J. Appl. Phys.* **114** 203908
- [37] Tiantian H and Lingyun Y 2013 Simulation optimization of performance for extraordinary magnetoresistance sensor in low-field *IEEE 11th Int. Conf. on Electronic Measurement and Instruments* p 636
- [38] Huang T, Ye L, Song K and Deng F 2014 Planar structure optimization of extraordinary magnetoresistance in semiconductor-metal hybrids *J. Supercond. Nov. Magn.* **27** 2059
- [39] Hewett T H and Kusmartsev F V 2010 Geometrically enhanced extraordinary magnetoresistance in semiconductor-metal hybrids *Phys. Rev. B* **82** 212404
- [40] Pugsley L M, Ram-Mohan L R and Solin S A 2013 Extraordinary magnetoresistance in two and three dimensions: geometrical optimization *J. Appl. Phys.* **113** 064505
- [41] Erlandsen R, Bjørk R, Kornblum L, Pryds N and Christensen D V 2022 Symmetry breaking in magnetoresistive devices *Phys. Rev. B* **106** 014408
- [42] Hewett T H and Kusmartsev F V 2009 Extraordinary magnetoresistance in hybrid semiconductor-metal systems *Int. J. Mod. Phys. B* **23** 4158
- [43] Sun J and Kosel J 2013 Influence of semiconductor/metal interface geometry in an EMR sensor *IEEE Sens. J.* **13** 664
- [44] Zhou T, Solin S and Hines D 2001 Extraordinary magnetoresistance of a semiconductor-metal composite van der Pauw disk *J. Magn. Magn. Mater.* **226–230** 1976

- [45] Umansky V, Heiblum M, Levinson Y, Smet J, Nübler J and Dolev M 2009 MBE growth of ultra-low disorder 2DEG with mobility exceeding $35 \times 10^6 \text{ cm}^2/\text{Vs}$ *J. Cryst. Growth* **311** 1658
- [46] Solin S A, Hines D R, Rowe A C H, Tsai J S and Pashkin Y A 2003 Nanoscopic magnetic field sensor based on extraordinary magnetoresistance *J. Vac. Sci. Technol. B* **21** 3002
- [47] Möller C, Grundler D, Kronenwerth O, Heyn C and Heitmann D 2003 Effect of the interface resistance on the extraordinary magnetoresistance of semiconductor/metal hybrid structures *J. Supercond.* **16** 195
- [48] Holz M, Kronenwerth O and Grundler D 2005 Semiconductor-metal hybrid structures as local magnetic-field probes: magnetoresistance and spatial sensitivity profile *Appl. Phys. Lett.* **87** 172501
- [49] Pooley O J, Gilbertson A M, Buckle P D, Hall R S, Buckle L, Emeny M T, Fearn M, Cohen L F and Ashley T 2010 Transport effects in remote-doped $\text{InSb}/\text{Al}_x\text{In}_{1-x}\text{Sb}$ heterostructures *New J. Phys.* **12** 53022
- [50] Lin B J F, Tsui D C, Paalanen M A and Gossard A C 1984 Mobility of the two dimensional electron gas in $\text{GaAs} - \text{Al}_x\text{Ga}_{1-x}\text{As}$ *Appl. Phys. Lett.* **45** 536–41
- [51] Makino T, Segawa Y, Tsukazaki A, Ohtomo A and Kawasaki M 2005 Electron transport in ZnO thin films *Appl. Phys. Lett.* **87** 22101
- [52] Tsukazaki A *et al* 2005 Repeated temperature modulation epitaxy for p-type doping and light-emitting diode based on ZnO *Nat. Mater.* **4** 42–46
- [53] Falson J, Kozuka Y, Uchida M, Smet J H, Arima T-H, Tsukazaki A and Kawasaki M 2016 MgZnO/ZnO heterostructures with electron mobility exceeding $1 \times 10^6 \text{ cm}^2/\text{Vs}$ *Sci. Rep.* **6** 26598
- [54] Mikheev E, Himmetoglu B, Kajdos A P, Moetakef P, Cain T A, Van de Walle C G and Stemmer S 2015 Limitations to the room temperature mobility of two-and three-dimensional electron liquids in SrTiO_3 *Appl. Phys. Lett.* **106** 62102
- [55] Yue J, Ayino Y, Truttmann T K, Gastiasoro M N, Persky E, Khanukov A, Lee D, Thoutam L R, Kalisky B and Fernandes R M 2021 Anomalous transport in high-mobility superconducting SrTiO_3 thin films (arXiv:2107.10904)
- [56] Irvin P, Veazey J P, Cheng G, Lu S, Bark C-W, Ryu S, Eom C-B and Levy J 2013 Anomalous high mobility in $\text{LaAlO}_3/\text{SrTiO}_3$ nanowires *Nano Lett.* **13** 364
- [57] Sing M *et al* 2009 Profiling the interface electron gas of LaAlO_3 - SrTiO_3 heterostructures with hard x-ray photoelectron spectroscopy *Phys. Rev. Lett.* **102** 176805
- [58] Christensen D V, Frenkel Y, Schütz P, Trier F, Wissberg S, Claessen R, Kalisky B, Smith A, Chen Y Z and Pryds N 2018 Electron mobility in $\gamma - \text{Al}_2\text{O}_3/\text{SrTiO}_3$ *Phys. Rev. Appl.* **9** 54004
- [59] Chen Y Z *et al* 2013 A high-mobility two-dimensional electron gas at the spinel/perovskite interface of $\gamma - \text{Al}_2\text{O}_3/\text{SrTiO}_3$ *Nat. Commun.* **4** 1371
- [60] Purdie D, Pugno N M, Taniguchi T, Watanabe K, Ferrari A C and Lombardo A 2018 Cleaning interfaces in layered materials heterostructures *Nat. Commun.* **9** 536–41
- [61] Wang L *et al* 2013 One-dimensional electrical contact to a two-dimensional material *Science* **342** 614
- [62] Yazdi-Rizi M, Marsik P, Mallett B P, Dubroka A, Christensen D V, Chen Y, Pryds N and Bernhard C 2016 Infrared ellipsometry study of the confined electrons in a high-mobility $\gamma - \text{Al}_2\text{O}_3/\text{SrTiO}_3$ heterostructure *Europhys. Lett.* **113** 47005
- [63] Schaefer B T, Wang L, Jarjour A, Watanabe K, Taniguchi T, McEuen P L and Nowack K C 2020 Magnetic field detection limits for ultraclean graphene hall sensors *Nat. Commun.* **11** 4163